Analytica Chimica Acta 1138 (2020) 59–68

Contents lists available at ScienceDirect

Analytica Chimica Acta

journal homepage: www.elsevier.com/locate/aca

# An enzyme-free electrochemical biosensor based on target-catalytic hairpin assembly and Pd@UiO-66 for the ultrasensitive detection of microRNA-21

Tianjiao Meng [a], Ningzhao Shang [b], Anaclet Nsabimana [c], Huimin Ye [a], Huan Wang [a], Chun Wang [b, **], Yufan Zhang [a, *]

[a] Key Laboratory of Medicinal Chemistry and Molecular Diagnosis of the Ministry of Education, Key Laboratory of Analytical Science and Technology of Hebei Province, College of Chemistry and Environmental Science, Institute of Life Science and Green Development, Hebei University, 071002, Baoding, PR China

[b] College of Science, Hebei Agricultural University, 071001, Baoding, PR China

[c] Chemistry Department, College of Science and Technology, University of Rwanda, Po Box: 3900, Kigali, Rwanda

## HIGHLIGHTS

- The sensitive electrochemical biosensor is constructed for the detection of miR-21 based on CHA and Pd@UiO-66.
- This biosensor shows low LOD and wide dynamic correlation of miR-21, providing a powerful platform for detecting miR-21.
- This method is enzyme-free, PCR-free, and convenient without the requirement of any additional separation steps.

## GRAPHICAL ABSTRACT

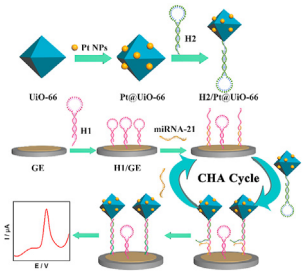


## ARTICLE INFO

*Article history:*
Received 20 July 2020
Received in revised form
9 September 2020
Accepted 10 September 2020
Available online 12 September 2020

*Keywords:*
MicroRNA-21
Electrochemical biosensor
Pd@metal-organic frameworks
Catalytic hairpin assembly

## ABSTRACT

MicroRNA-21 (miR-21) has been widely investigated as important biomarkers for cancer diagnosis and treatment. Herein, a highly sensitive nonenzymatic electrochemical biosensor based on Pd@metal-organic frameworks (Pd@UiO-66) and target-catalytic hairpin assembly (CHA) with target recycling approach has been proposed for the detection of miR-21. The proposed biosensor integrates the efficient CHA strategy and excellent electrocatalytic performance of Pd@UiO-66 nanocomposites. The concentration of miRNA-21 is related to the amount of the adsorbed electrocatalyst, leading to the different electrochemical signals for readout towards paracetamol (AP). This biosensor shows a low limit of detection of 0.713 fM with the dynamic range of 20 fM –600 pM under the optimal experimental conditions, providing a powerful platform for detecting miR-21. Furthermore, the designed biochemical self-assembly strategy of this electrochemical biosensor is promising candidate for potential applications in the analysis of other important genetic biomarkers for early diagnosis of cancers.



## 1. Introduction

MicroRNA, a kind of small non-coding ribonucleic acids (RNA) that regulate over 30% of human genome, are extensively involved

* Corresponding author.
** Corresponding author.
*E-mail addresses:* wangchun@hebau.edu.cn (C. Wang), zyf@hbu.edu.cn (Y. Zhang).

https://doi.org/10.1016/j.aca.2020.09.022
0003-2670/

in almost every cellular process including cell differentiation, genetic expression, biological development and cancer disease diagnosis [1–4]. MicroRNA-21 (miR-21) is an oncogenic microRNA that regulates the expression of various genomes. The over-expression of miR-21 can lead to various diseases, such as tumorigenesis, cardiovascular diseases, kidney diseases, and cancers, making miR-21 a valuable biomarker in clinical diagnosis and prognostic of cancers [5–9]. Therefore, sensitive and selective analytical method for the rapid and accurate determination of miR-21 is of significant importance in biomedical research.

Electrochemical methods have recently been extensively utilized in the analysis of various biological molecules owing to their advantages including high sensitivity, low cost, fast, and easy operation, etc. [10–15]. Two approaches for fabrication of electrochemical miRNA biosensor have been reported. Label-free and reagentless electrochemical miRNA biosensors are the most widely used techniques because of the rapid, simple, high sensitivity, and high sequence selectivity [16–19]. Recently, labeled and indirect electrochemical miRNA biosensors have been applied within studies for miRNA detection [20–22]. Various nanomaterials such as noble metal nanoparticles, magnetic nanoparticles, and quantum dots can be strong tools to improve performances of classical detection methods [23–27]. The high-efficiency nucleic acid signal amplification strategy has become one of the most attractive strategies to further improve the sensitivity of the electrochemical analysis techniques. At present, various isothermal nucleic acid amplification strategies for miRNA detection have been developed, including loop-mediated isothermal amplification (LAMP), strand displacement amplification (SDA), rolling circle amplification (RCA), target-catalyzed hairpin assembly (CHA) and hybridization chain reaction (HCR) [28–33].

In a typical CHA reaction, the nucleic acid hybridization is utilized as energy to drive the DNA hairpin structure to assemble continuously. Recently, an enzyme-free amplification approach based on CHA has attracted wide attention and extensively utilized in the miRNA analysis due to its high sensitivity, simplified conditions of detection, and short analysis time [7,9,34]. Furthermore, the recycling target can greatly improve the sensitivity of the biosensor.

Metal-organic frameworks (MOFs) fabricated by combining inorganic metal ions/clusters and organic linkers have demonstrated extraordinary performances in many fields because of their well-defined porosities, high thermal stability, large surface area, and chemical tunability [35–37]. Their structural and functional tunability makes them compelling candidates for many applications including heterogeneous catalysis, sensing, energy harvesting, gas adsorption, and biomedicine [38–45]. Specifically, MOFs have drawn increasing attention in electrochemical applications owing to their different and controlled surface area, pore size, and surface functionality. In addition, the specific functions of MOFs can be endowed through the precise chemical modification that enables them to promote developments in many areas. Noble-metal nanoparticles have attracted wide attention in heterogeneous catalysis because of their extraordinary properties [46–49]. In general, MOFs can act as supporting materials for loading noble-metal nanoparticles owing to their high volume fraction of active metal sites, controllable topologies, and high porosities [50]. These unique properties result in the improved dispersity of nano-entities.

In this work, we have fabricated an enzyme-free and PCR-free electrochemical biosensor based on CHA strategy and Pd/MOFs (Pd@UiO-66, UiO = Universitetet i Oslo) nanocomposite for miR-21 detection. An illustration of sensing principle for the electrochemical detection of miR-21 is shown in Scheme 1. The surface of gold electrode (GE) surface was modified with hairpin capture probe (H1) via the conjugating −SH groups of H1 and GE. Meanwhile, the detection probe with tracing tags of H2/Pd@UiO-66 was formed via the incubation between Pd@UiO-66 nanocomposite and H2 through specific bonds between −COOH groups of H2 and $-NH_2$ groups of Pd@UiO-66. According to hybridization principle of DNA, the stem of H1 was opened and exposed its concealed sequence by introducing the target miR-21. Subsequently, the target miR-21 was released through the hybridized between H1-miR-21 complex and H2. Meanwhile, a plenty of H2 was captured in the next cycle via the released target miR-21. Electrochemistry, as a powerful tool, has been designed to detect biomolecules. As miRNAs do not have redox properties, the electrochemical detection of miRNAs can be achieved via indirect method. Therefore, as an electroactive substance, paracetamol (AP) can be used for indirect detection of miR-21. More concretely, the concentration of miRNA-21 is related to the amount of the adsorbed electrocatalyst, leading to the different electrochemical signals for readout towards AP. Importantly, the proposed Pd@UiO-66 nanocomposite has prepared via a simple and rapid one-step hydrothermal method, which not only shortens the preparation time of biosensor but also enhances the electrochemical response. In addition, a GE has been employed in this biosensor. Comparing with the typical glassy carbon electrode, the GE could capture DNA via the conjugating −SH groups of H1 and GE (Au−S bonds). Therefore, the proposed electrochemical biosensor provided a novel avenue for the detection of other biomarkers. As a result, based on the CHA between H2/Pd@UiO-66 and H1/GE, the designed protocol can obtain a significantly amplified electrocatalytic current towards AP and provides a sub-femtomolar level for miR-21 assay.

## 2. Experimental

### 2.1. Chemicals and materials

All the HPLC purified DNAs and miRNAs were received from Sangon, Inc. (Shanghai, China) and are listed in Table S1. Gelred and loading buffer were purchased from Sangon, Inc. (Shanghai, China). Acrylamide and diethyl pyrocarbonate (DEPC) were obtained from Biosharp, Inc. (Hefei, China). Ammonium persulphate, N-(3-dimethylaminopropyl)-N-ethylcarbodiimidehydrochloride (EDC, 98%), tris-HCl, tris (2-carboxyethyl) phosphine, and N-hydroxysuccinimide (NHS, 98%) were provided by Aladdin, Inc. (Shanghai, China). *N,N,N′,N′*-Tetramethylethylenediamine (TEMED) was purchased from Sigma-Aldrich, Inc. (Beijing, China). *N, N′*-dimethylformamide (DMF), zirconium chloride ($ZrCl_4$, 98%, analytical grade), $PdCl_2$, 2-aminoterephthalic acid ($NH_2$−$H_2$BDC, analytical grade), acetic acid (HAc), 6-Mercapto-1-hexanol (MCH), HCl, orthoboric acid, trichloromethane ($CHCl_3$), isopropanol, and AP were purchased from MACKLIN Reagent Co. Ltd. Deionized water and DEPC were used in this study.

### 2.2. Apparatus

Electrochemical impedance spectroscopy (EIS) was studied using an AUTOLAB Electrochemical Workstation (Metrohm Instruments, Switzerland). Cyclic voltammetry (CV) and differential pulse voltammetry (DPV) were investigated using a CHI760E electrochemical workstation (Shanghai Chenhua Instrument). The morphologies of the nanocomposites were analyzed by scanning electron microscope (SEM, JSM-7500F, Japan) and transmission electron microscope (TEM, JEM-2100F, Japan). X-Ray diffraction (XRD) patterns of samples were carried out on an X-ray D/max-2200vpc instrument (Rigaku Corporation, Japan). Energy dispersive X-ray (EDX) spectra were obtained by a JEM-2100 F TEM JEOL (Japan) operating at 200 kV. $N_2$ adsorption-desorption isotherms

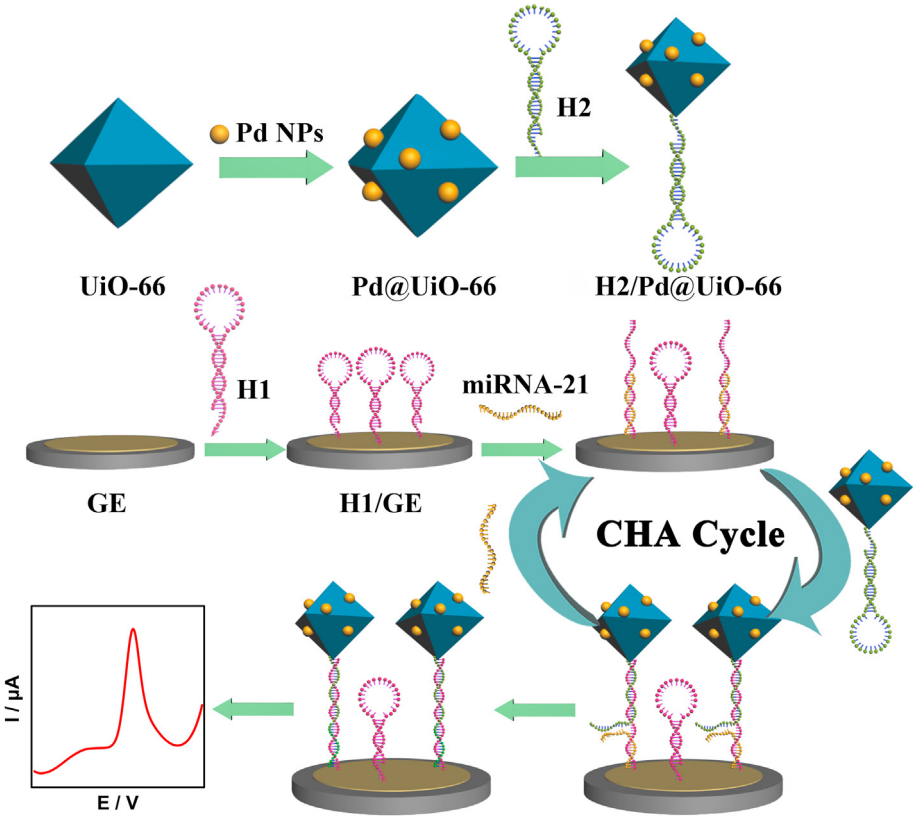


**Scheme 1.** A principle of electroanalytical method for detecting miR-21 based on target-CHA and Pd@UiO-66.

were carried out by AutosorbiQASIQ (Quantachrome, USA). The surface functional types of materials were investigated by Fourier transform infrared (FT-IR) spectroscopy on a Nicolet Magna 560 FT-IR spectrometer. Thermogravimetric analysis (TGA) was performed on a PerkinElmer Diamond TG analyzer. Zeta potential was investigated by Zeta Potential Analytical Instruments (Brookhaven Instruments, USA).

### 2.3. Extraction of total RNA in cells

The total RNA was extracted from breast cancer cell (MCF-7), cervical cancer cell (HeLa), non-small cell lung cancer cell (A549), mouse leukemia cells of monocyte-macrophage (RAW 264.7) and human umbilical vein endothelial cells (HUVEC). In brief, 200 μL of $CHCl_3$ was added into a non-enzymatic centrifuge tube containing about $1 \times 10^6$ cells. Then, the cells were centrifuged at 12,000 rpm for 14 min at 4 °C. Next, the supernatant was washed with isopropanol and then centrifuged at 12,000 rpm for 10 min at 4 °C. Then, the supernatant was washed with ethanol and centrifuged at 9500 rpm for 5 min at 4 °C. At last, the total RNA was dispersed in 15 μL of DEPC and stored at −70 °C before utilization.

### 2.4. Preparation of Pd@UiO-66

The hydrothermal method with minor modifications was applied to prepare the Pd@UiO-66 nanocomposites [51]. Firstly, 1.64 g of $ZrCl_4$ and 1.16 g of $H_2BDC\text{-}NH_2$ were added in 80 mL of DMF with stirring constantly. Next, 0.5 mL of deionized water and 12 mL HAc were added to this mixture with magnetic stirring for 10 min. After that, the mixture was transferred to a Teflon liner and placed in a drying oven at 120 °C for 24 h. Subsequently, the mixture was purified by washing with DMF and ethanol for 3 times with centrifugation before drying at 60 °C for 6 h. Then, the mixture of the as-prepared 1 g of UiO-66 and 4 mL of $PdCl_2$ (8.325 mg $mL^{-1}$) was ultrasonicated for 12 h. Next, the obtained Pd@UiO-66 solution was dried slowly at room temperature (25 °C) for 48 h. Finally, the Pd@UiO-66 was dried at 152 °C for 12 h. The photos of pure UiO-66 and Pd@UiO-66 composites are observed in Fig. S1.

### 2.5. Preparation of H2/Pd@UiO-66

To activate H2, 200 μL of H2 (2.5 μM) was transferred into 200 μL of the solution of EDC/NHS (4/1), and the resulting solution was kept for 60 min. Then, 500 μL of Pd@UiO-66 composite dispersion (Pd@UiO-66 dispersed in 0.1 M of PBS 7.4, 1 mg $mL^{-1}$) was slowly added into the above solution and reacted at 4 °C for 8 h. To remove the excess reagents, the mixture was centrifuged for 10 min at 10,000 rpm. The H2/Pd@UiO-66 was formed via the $-NH_2$/-COOH affinity between Pd@UiO-66 and H2. The obtained H2/Pd@UiO-66 was redissolved in 0.1 M of PBS (pH 7.4) and kept at 4 °C before use.

### 2.6. Fabrication of the miR-21 sensing platform

A conventional three-electrode system, consisting of a GE (2 mm diameter) as working electrode, an Ag/AgCl (saturated KCl) as the reference electrode and a platinum wire as counter electrode, was used. First, the bare GE was carefully polished with slurry of alumina (0.3 and 0.05 μm). Then, the GE was washed again in ethanol and deionized water by sonication. Afterwards, the GE was incubated in 2.5 μM of H1 at 4 °C for 10 h. To remove the physically adsorbed H1, the modified GE was rinsed with deionized water. Next, 6 μL MCH (1 mM) were dropped onto the surface of the as-prepared GE and kept at 4 °C for 1 h. Then, the modified GE was rinsed thoroughly with deionized water. For electrochemical

detection, the mixture (20 μL) of H2/Pd@UiO-66/miR-21 standard solution (1/1) was drop-coated onto the modified GE and incubated at 37 °C for 90 min. Finally, the surface of the obtained sensor was washed with deionized water, followed by drying in nitrogen gas and stored in air before utilization.

## 3. Results and discussion

### 3.1. Characterization of the UiO-66 and Pd@UiO-66 composites

The morphological character and microstructure of the UiO-66 and Pd@UiO-66 were initially investigated with TEM images. Fig. 1 (A and B) show the regular octahedal crystal shapes of UiO-66. Compared with pure UiO-66, many Pd NPs are uniformly distributed on Pd@UiO-66 (Fig. 1 (D and E)). It also indicates that the regular octahedal crystal structure of UiO-66 host is maintained after the loading of Pd NPs. Furthermore, UiO-66 and Pd@UiO-66 exhibit intact crystal morphology with 135 nm, which confirm that there is no transformation or deformity of the UiO-66 framework after the incorporation of Pd NPs on the support (Fig. S3). The components of samples were indicated using EDX spectra [43–45,52,53]. In Fig. 1C, the peaks of EDX spectrum correspond to C, O, Cl and Zr elements for pure UiO-66. The EDX spectrum of Pd@UiO-66 exhibits the peaks corresponding to C, O, Zr, Cl and Pd elements (Fig. 1F), confirming the successful preparation of Pd@UiO-66 composite (the peaks of Cu element coming from copper grid). The EDX spectra also indicate the quantitative elemental analysis in wt%: C 37, O 15, Cl 3 and Zr 31 in pure UiO-66; C 46, O 13, Cl 5, Zr 20 and Pd 2 in Pd@UiO-66. The EDX mapping reveals that C, O, Zr, Cl and Pd elements are homogeneously distributed throughout the nanopolyhedral frameworks (Fig. 1G). This is in good agreement with the TEM analysis, confirming that the successful preparation of Pd@UiO-66 composite.

In addition, the FT-IR spectra were investigated to confirm the structure of nanocomposites (Fig. 2A). The peaks at 3350-3500 $cm^{-1}$ can be assigned to the −OH asymmetric stretching vibration [54]. The peaks at 1255 and 2940 $cm^{-1}$ can be assigned to the C−$NH_2$ stretching vibration and the C−H asymmetric stretching vibration, which indicates the presence of the amine groups within the framework of UiO-66 and Pd@UiO-66 [55]. The intensity of the two peaks becomes weaker after the loading of Pd, suggesting that there is an interaction between Pd and the −$NH_2$ groups. The peak

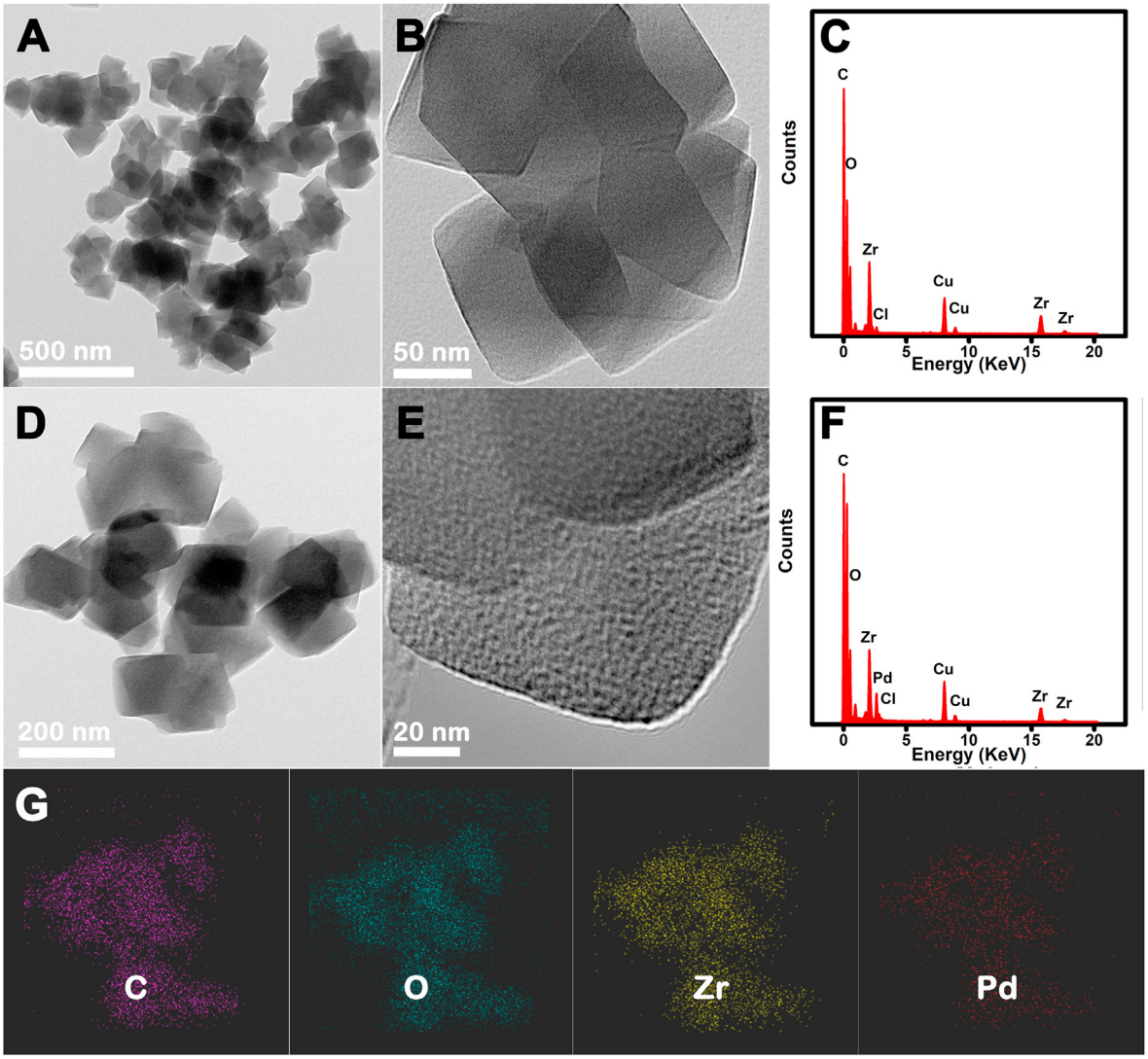


**Fig. 1.** TEM images (A and B) and EDX spectrum (C) of pure UiO-66, TEM images (D and E) and EDX spectrum (F) of Pd@UiO-66, EDX mapping of Pd@UiO-66 composite for C, O, Zr, and Pd elements (G).

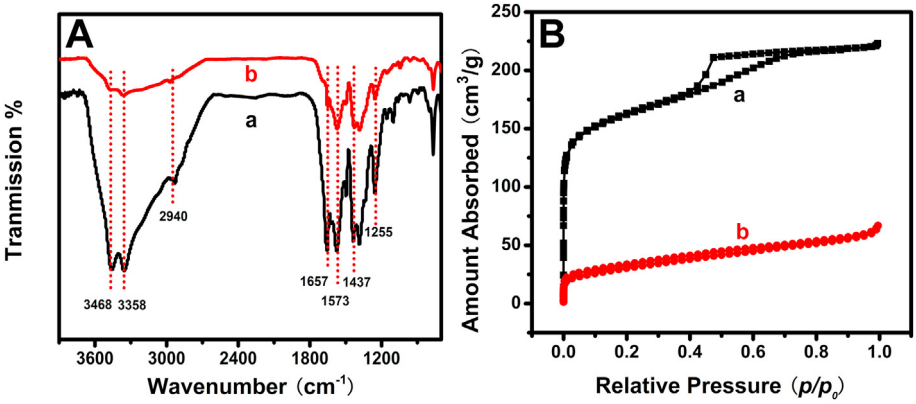


**Fig. 2.** FT-IR spectra of UiO-66 (a) and Pd@UiO-66 (b) (A). $N_2$ adsorption-desorption isotherms of UiO-66 (a) and Pd@UiO-66 (b) (B).

at 1657 $cm^{-1}$ on the Pd@UiO-66 spectrum can be assigned to the C—O scissoring vibrations, which originates from small amounts of the residual DMF in UiO-66 [56]. Interestingly, it disappears in the curve of Pd@UiO-66, which implies that the residual DMF can be thoroughly removed during the preparation process for the loading of Pd. The presence of bands at 1437 $cm^{-1}$ and 1573 $cm^{-1}$ of the nanocomposites results from the stretching mode of COO- groups [57].

$N_2$ adsorption-desorption isotherms were employed to achieve the profile insights about the materials (Fig. 2B). According to the results of Brunauer-Emmett-Teller (BET) method, the pure UiO-66 exhibits high surface area of 873.6 $m^2\ g^{-1}$. The surface area of Pd@UiO-66 (126 $m^2\ g^{-1}$) is decreased because the portion of the cavities are occupied by the deposited Pd species.

The thermal stability of pure UiO-66 support and Pd@UiO-66 catalysts were investigated using TGA (Fig. S2). A small weight loss peak is observed between 40 °C and 160 °C, likely ascribed to the removal of chemically adsorbed $H_2O$. An obvious weight loss peak is observed between 335 °C and 525 °C, which corresponds to the complete decomposition of the organic linkers in inert atmosphere.

The XRD results of UiO-66 and Pd@UiO-66 composites with octahemioctahedral crystal structure are shown in Fig. S4. The XRD curves show the peaks at 14.48, 17.08, 19.16, 22.38, 25.18, and 30.88°, corresponding (222), (400), (420), (511), (600), and (640) of the standard patterns of UiO-66 (JCPDF card number: 36—1452). From curve b, no significant loss of crystallinity is detected, which demonstrates that incorporation of Pd NPs does not disrupt or destroy the crystal structure of UiO-66. Meanwhile, the absence of XRD peaks from Pd NPs may be attributed to the small size of encapsulated Pd NPs in the UiO-66 framework.

### 3.2. Native polyacrylamide gel electrophoresis

Polyacrylamide gel electrophoresis (PAGE) was employed to confirm the feasibility of the biochemical self-assembly process (Fig. S5). A well-defined band at lane 1 (hairpin H1), lane 2 (hairpin H2) and lane 3 (miR-21) can be clearly observed. A lower migration rate band is obtained because of a higher molecular weight of hairpin H1 compared with hairpin H2. Simultaneously, a distinct dual-band (lane 4: loaded with the mixture of H1 and H2) can be observed, which indicates that no hybridization occurred between H1 and H2 in absence of miR-21. In contrast, the band of the mixture of hairpin H1, hairpin H2 and miR-21 was observed with a lower migration rate compared with the reaction species (lane 5). Therefore, the PAGE results illustrated the feasibility of the designed CHA reaction.

### 3.3. Electrochemical behavior of different electrode materials

The EIS technique was utilized to investigate the assembly processes on the electrode surface. Fig. 3A shows the EIS results, which corresponded to each modification step on the surface of GE surface. After the immobilization of DNA, it is expected that the impedance increases because of the oligonucleotides with negatively charged repelling $[Fe(CN)_6]^{3-/4-}$ ions form spatial blockage. As expected, curve a exhibits a relatively low $R_{ct}$ of 145.7 ± 1.33% Ω, corresponding to the fast charge-transfer process on bare GE. The GE immersed in H1 (curve b) exhibits a higher $R_{ct}$ (215.3 ± 1.65% Ω) than that of bare GE since the repellence of $[Fe(CN)_6]^{3-/4-}$ from the electrode approached by the abundant negatively charged DNA backbones. MCH can shield the active site of the exposed Au due to their non-electroactive performance. As expected, the $R_{ct}$ value (423.6 ± 0.447% Ω) of curve c is increased obviously when the H1 GE is passivated with MCH, which can be ascribed to the fact that MCH hindered the electron transfer. After that, H2/Pd@UiO-66 (curve d) modified MCH/H1/GE exhibits an increased $R_{ct}$ of 2171 ± 0.327% Ω. After the connection with miR-21 (curve e), the $R_{ct}$ value is 3035 ± 0.370% Ω. The change of $R_{ct}$ values confirmed the successful assembly processes of the electrochemical biosensor, which is consistent with the results of PAGE.

Furthermore, zeta potential was employed to confirm the successful preparation of H2/Pd@UiO-66 (Fig. S6). The zeta potential of the prepared Pd@UiO-66 is 18.2 mV. Due to the abundant phosphate groups of oligonucleotides, the zeta potential of H2/Pd@UiO-66 turned into 7.99 mV, which proved that the H2/Pd@UiO-66 conjugates had been successfully synthesized.

DPV measurements were used to further verify the electrocatalytic performance of the biosensors in PBS (pH = 7.4). Fig. 3B shows the electrochemical behavior of different electrodes towards AP oxidation. For MCH/H1/GE (curve a), no obvious oxidation peak current is observed because the MCH could block the nonspecific adsorption sites. For the H2/Pd@UiO-66/GE (curve b), a small oxidation peak current could be observed, which might be assigned to the nonspecific adsorption between the H2/Pd@UiO-66 and GE. For the curve c of Fig. 3B, an obvious oxidation peak current is observed, which might be attributed to the hybridization between H2/Pd@UiO-66 and H1 in the presence of miR-21. Briefly, a large number of H1/H2/Pd@UiO-66 were formed through the hybridization reaction between H2/Pd@UiO-66 and H1 containing the target miR-21. Subsequently, the released target miR-21 further acted as triggers for the next chain hybridization process. After the cyclic amplification process, a large number of H1/H2/Pd@UiO-66 duplex were formed on the GE surface, which could directly generate an oxidation signal for AP.

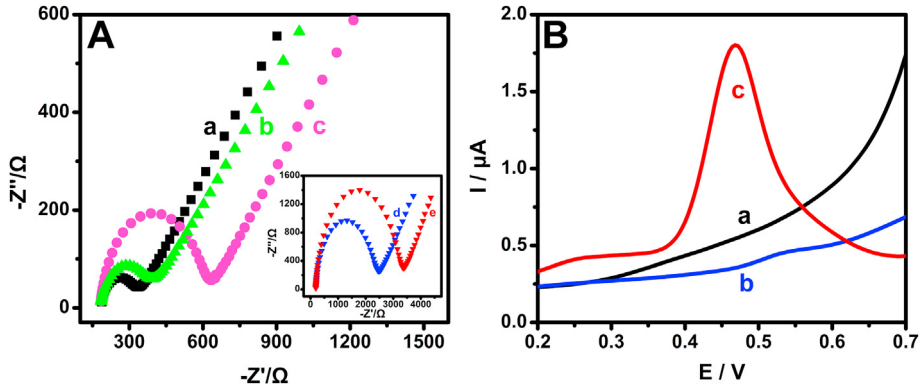


**Fig. 3.** Nyquist plots of EIS for the different modified electrodes in 0.1 M of KCl containing 5.0 mM of $Fe[(CN)_6]^{4-/3-}$ solution: bare/GE (a), H1/GE (b), MCH/H1/GE (c), MCH/H1/H2/Pd@UiO-66/GE (d), MCH/H1/H2/Pd@UiO-66/miR-21/GE (e) (A). DPV curves of MCH/H1/GE (a), MCH/H1/H2/Pd@UiO-66/GE (b), MCH/H1/H2/Pd@UiO-66/miR-21/GE (c) in PBS (pH = 7.4, 0.1 M) containing 0.5 mM of AP, potential: 0.2–0.7 V (B).

### 3.4. Optimization of the detection conditions

To achieve high sensitivity and hybridization efficiency, the influence of the concentrations of H1 and H2 probes, incubation time of H1-GE, and hybridization time were investigated. The effect of concentrations of H1 probe was studied (Fig. 4A). The largest current value was obtained when the concentration of H1 was 2.5 μM. In addition, with the further increase of the concentrations of H1, the current value decreased gradually, suggesting the excess of H1 can block the hybridization of miR-21. As seen from Fig. 4B, with the increased of the concentrations of H2, the current value reached a platform at 2.5 μM of H2. Thus, 2.5 μM was selected as the optimal concentration of H1 and H2. Fig. 4C shows that the current signals increased with the incubation time from 2 to 10 h and remained stable when the incubation time was prolonged from 10 to 16 h. As a result, 10 h was selected as the best incubation time for the hybridization reaction between H1 probe and GE. The hybridization time was also optimized by incubating miR-21 with H1 and H2/Pd@UiO-66 from 20 to 120 min (Fig. 4D). Results showed that the peak current value increased with the increasing hybridization time and reached a maximum value at 80 min. Therefore, 80 min was chosen as the optimal time for the hybridization.

### 3.5. Electrochemical detection of miR-21

The DPV measurements were employed to assess the electrochemical behavior of as-prepared miR-21 biosensor. Fig. 5A illustrates the DPV response signals for target miR-21 under the optimal conditions. Displayed by response currents, the electrochemical signals increased linearly with the successively increasing

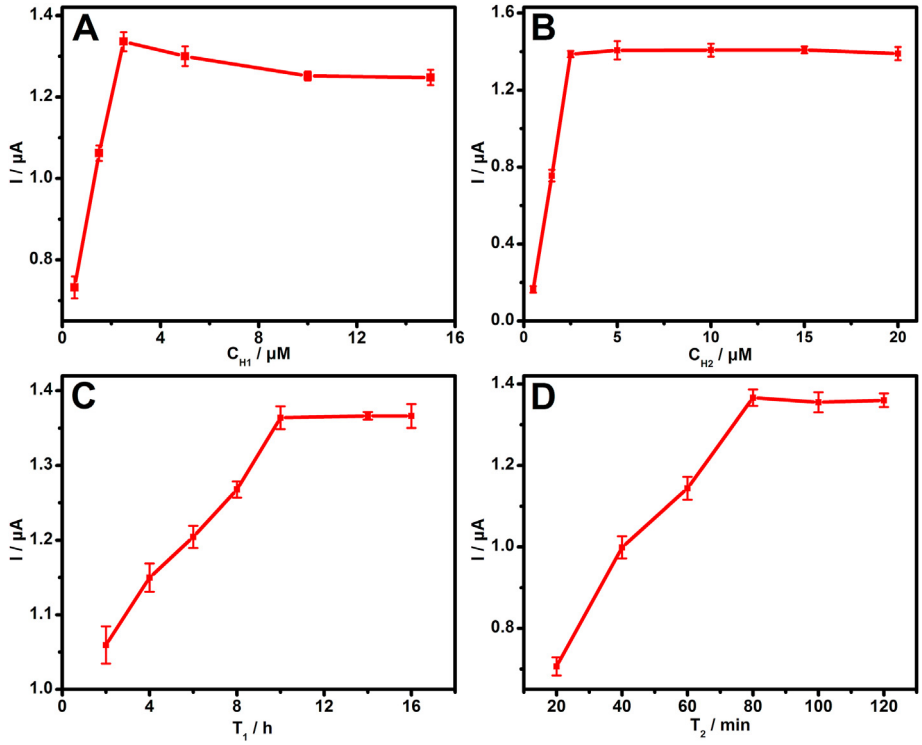


**Fig. 4.** Influence of concentrations of H1 (A) and H2 (B), incubation time of hybridization reaction between H1 and GE (C), hybridization reaction time between H2/Pd@UiO-66 and H1 (D) on DPV response currents with 0.1 nM of miR-21; DPV response of modified GE in PBS (pH = 7.4, 0.1 M) containing 0.5 mM of AP in different conditions, potential: 0.2–0.7 V.

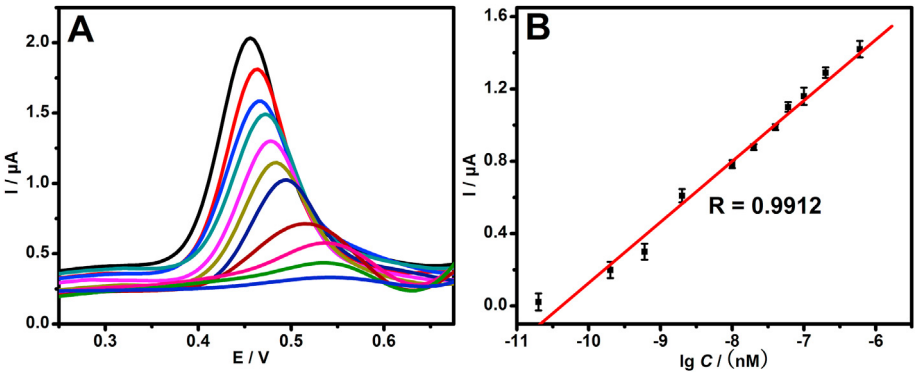


**Fig. 5.** DPV curves for target miR-21 at different concentrations (0, 20 fM, 200 fM, 600 fM, 2 pM, 20 pM, 40 pM, 60 pM, 100 pM, 200 pM, and 600 pM) in PBS (pH = 7.4, 0.1 M) containing 0.5 mM of AP in different conditions, potential: 0.2–0.7 V (A). The calibration curve between the values of DPV peak current and the logarithm of miR-21 concentrations (B).

**Table 1**
Comparison between the proposed strategy and other methods for detection of miRNA.

| Materials | Analytical technique | Linear range | Sensitivity ($\mu A \mu M^{-1}$) | Limit of detection (fM) | References |
|---|---|---|---|---|---|
| CdTe nanocrystals and Au nanoclusters[a] | ECL[b] | 100 fM–100 nM | – | 21.7 | [58] |
| amplification products/MCH/Cp[c] | SWV[d] | 2 fM–500 pM | 165.7 | 1.6 | [59] |
| Au-g-$C_3N_4$ NH[e] | ECL | 1 fM –1 nM | – | 0.5 | [60] |
| Electrode-free | Colorimetric | 0–0.1 nM | 450 | 32 | [61] |
| HP/CNTs/GCE[f] | DPV | 10 fM–100nM | 350 | 1.2 | [62] |
| Au nanoparticles | Fluorescence | 3.8 pM–10 nM | – | 3.8 | [63] |
| Au@NPFe$_2$O$_3$NC[g] | DPV | 500 fM–5 nM | 3.375 | 100 | [64] |
| Arched Probe Mediated Isothermal Exponential Amplification | DPV | 20 fM–10 nM | 274.2 | 5.36 | [65] |
| MBA-AuNPs/DA-AuNPs[h] | DPV | 100 fM–10 pM | 53 | 45 | [66] |
| $MoS_2$-Thionine-AuNPs[i] | SWV | 1 pM–10 nM | 204 | 260 | [67] |
| Hairpin capture probe/target recycling/MB[j] | DPV | 0.5 pM–2 nM | 300.6 | 56 | [68] |
| **Pd@UiO-66** | **DPV** | **20 fM–600 pM** | **336** | **0.713** | **This work** |

[a] CdTe nanocrystals and Au nanoclusters modified on glassy carbon electrode.
[b] Electrochemiluminescence.
[c] Amplification products/6-Mercapto-1-hexanol/capture probe.
[d] Square wave voltammetry.
[e] Au nanoparticles functionalized g-$C_3N_4$ nanohybrid coated on glassy carbon electrode.
[f] Carbon nanotube -hairpin probe modified electrode.
[g] Gold-loaded nanoporous iron oxide nanocubes.
[h] 4-mercaptophenylboronic acid -capped Au nanoparticles/dopamine -capped Au nanoparticles.
[i] Thionine and gold nanoparticles co-functionalized $MoS_2$ nanosheet.
[j] Hairpin capture probe/target recycling/methyl blue.

concentration of target miR-21. The standard curve in Fig. 5B indicates the regression equation of $I(\mu A) = 0.336 \lg C\,(nM) + 3.49$ and a low limit of detection of 0.713 fM with a high correlation coefficient (R = 0.9912), which is comparable with or even superior to previously reported signal amplification strategies (Table 1).

### 3.6. Selectivity, stability, and reproducibility of the proposed biosensor

The selectivity, stability, and reproducibility of the biosensor were also studied to fully investigate the electrochemical biosensing platform. As shown in Fig. 6A, miRNAs including miR-141, miR-155, and miR-199A were employed to investigate the selectivity of the miR-21 biosensor. The DPV response signals of miR-141 (0.030 μA), miR-155 (0.050 μA), and miR-199A (0.056 μA) are similar to the blank reagents (0.025 μA). As expected, the obviously DPV response signal is observed for the samples containing target miR-21 (over 1.170 μA). These results are comparable with previous reports [69–73]. These results illustrate that the proposed electrode has high selectivity. Furthermore, the reproducibility was verified by incubating the miR-21 using the same sensor in the same conditions (n = 10). The results indicated the RSD of 4.04%, suggesting that the developed biosensor has excellent reproducibility. When the biosensor was stored in the fridge at 4 °C for 2 weeks, the signal intensity remained 91.4% (n = 10) of its initial value, indicating that the developed electrochemical biosensor has a long-term stability.

In addition, the proposed biosensor was used to detect the content of miR-21 derived from MCF-7, HeLa, A549, and RAW 264.7 cells (Fig. 6B). Apart from the four cancer cells, the HUVEC was served as an endogenous reference gene for normalization purposes. As expected, more significant current responses were obtained from MCF-7, HeLa, A549, and RAW 264.7 cell lines. The results proved the over expression of miR-21 in MCF-7, HeLa, A549, and RAW 264.7 cells.

### 3.7. Detection of target miRNA in real samples

To validate the feasibility of proposed biosensor, the recovery experiments were carried out by adding miR-21 (0.1 pM and 1 pM) to normal human serum samples (10-fold-diluted). Table 2 shows the recoveries, ranging from 96.2% to 110%, and the corresponding RSD, ranging from 0.59% to 5.12%. These results suggest that this assay has a good practicability for the detection of target miR-21 in real samples.

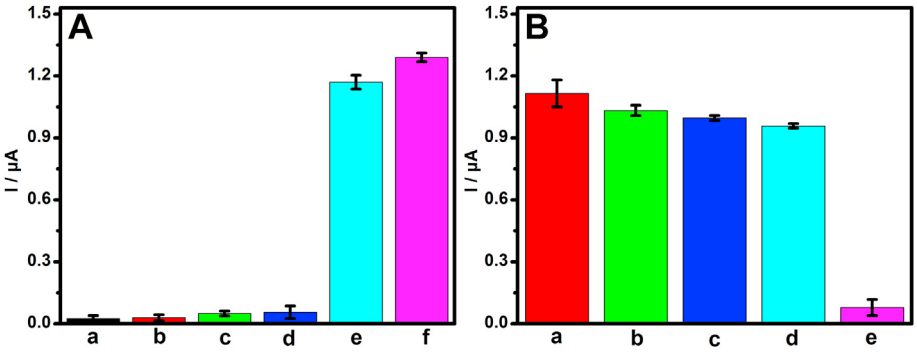


**Fig. 6.** Selectivity of the proposed biosensor for different miRNA sequences: blank (a), 10 pM of miR-155 (b), 10 pM of miR-141 (c), 10 pM of miR-199A (d), 1 pM of miR-21 (e), a mixture (containing miR-21, miR-155, miR-141 and miR-199A) (f) (A). The quantitative results of the proposed biosensor for miR-21 detection produced from MCF-7 (a), HeLa (b), A549 (c), RAW 264.7 (d), and HUVEC cells (e) (B). DPV response of MCH/H1/H2/Pd@UiO-66/miR-21/GE in PBS (pH = 7.4, 0.1 M) containing 0.5 mM of AP in different conditions, potential: 0.2–0.7 V.

**Table 2**
Determination of miR-21 (0, 0.1, and 1 pM) with the as-prepared biosensor in human serum samples (10-fold-diluted).

| Human serums | Samples | Added (pM) | Founded (pM) | Recovery (%) | RSD (%) |
|---|---|---|---|---|---|
| a | 1 | 0 | 0.630 | – | 1.97 |
| | 2 | 0.1 | 0.110 | 110 | 2.10 |
| | 3 | 1 | 1.02 | 102 | 4.35 |
| b | 1 | 0 | 0.150 | – | 3.78 |
| | 2 | 0.1 | 0.096 | 96 | 2.08 |
| | 3 | 1 | 1.05 | 105 | 0.590 |
| c | 1 | 0 | 1.30 | – | 3.47 |
| | 2 | 0.1 | 0.106 | 106 | 5.12 |
| | 3 | 1 | 0.105 | 105 | 4.46 |

## 4. Conclusion

In conclusion, the present work focuses on the construction of an ultrasensitive electrochemical biosensor for miR-21 detection based on Pd@UiO-66 as nanocatalyst and the CHA for signal application. Importantly, Pd@UiO-66 as an excellent electrocatalyst exhibits obvious effect of electrochemical signal amplification. Different electrochemical signals could be obtained by adsorbing the different amount of electrocatalyst. The readout response current positively correlated with miR-21 content, enabling the quantitative detection of miR-21 indirectly. The proposed biosensor integrates the efficient CHA strategy and excellent electrocatalytic performance of Pd@UiO-66 nanocomposites, leading to the remarkable signal enhanced electrochemical detection of miR-21. The proposed biosensor shows a low limit of detection of 0.713 fM with the dynamic range of 20 fM −600 pM. Furthermore, this biosensor illustrates high selectivity, excellent reproducibility, long-term stability, and good practicability. The over-expression of miR-21 can lead to various diseases and this makes miR-21 a valuable biomarker in clinical diagnosis and prognostic of cancer. Thus, the designed biochemical self-assembly strategy of this electrochemical biosensor would provide the great potential for analysis of other important genetic biomarkers, facilitating the early diagnosis of cancers.

## CRediT authorship contribution statement

**Tianjiao Meng:** Investigation, Methodology, Writing - original draft. **Ningzhao Shang:** Data curation, Software, Writing - original draft. **Anaclet Nsabimana:** Methodology, Writing - review & editing. **Huimin Ye:** Software, Data curation. **Huan Wang:** Writing - review & editing, Funding acquisition. **Chun Wang:** Investigation, Methodology, Data curation, Software. **Yufan Zhang:** Investigation, Methodology, Data curation, Software, Supervision, Funding acquisition.

## Declaration of competing interest

The authors declare that they have no known competing financial interests or personal relationships that could have appeared to influence the work reported in this paper.

## Acknowledgements

The authors gratefully acknowledge the support from the Priority Strategy Project of Key Laboratory of Medicinal Chemistry and Molecular Diagnosis of Ministry of Education (No. ts2019003), the Natural Science Foundation of Hebei Province (No. B2019201407 and No. B2018201214), the Science and Technology Research Project of Higher Education Institutions in Hebei Province (No. QN2020153), and the Advanced Talents Incubation Program of the Hebei University (No. 801260201026).

## Appendix A. Supplementary data

Supplementary data to this article can be found online at https://doi.org/10.1016/j.aca.2020.09.022.

## References

[1] L. Tian, K. Qian, J. Qi, Q. Liu, C. Yao, W. Song, et al., Gold nanoparticles superlattices assembly for electrochemical biosensor detection of MicroRNA-21, Biosens. Bioelectron. 99 (2017) 564–570.
[2] H. Shuai, K. Huang, Y. Chen, L. Fang, M. Jia, Au nanoparticles/hollow molybdenum disulfide microcubes based biosensor for microRNA-21 detection coupled with duplex-specific nuclease and enzyme signal amplification, Biosens. Bioelectron. 89 (2017) 989–997.
[3] J. Liu, Z. Tang, J. Zhang, Y. Chai, Y. Zhuo, R. Yuan, Morphology-controlled 9,10-

diphenylanthracene nanoblocks as electrochemiluminescence emitters for microRNA detection with one-step DNA walker amplification, Anal. Chem. 90 (2018) 5298–5305.
[4] Y. Wei, W. Zhou, X. Li, Y. Chai, R. Yuan, Y. Xiang, Coupling hybridization chain reaction with catalytic hairpin assembly enables non-enzymatic and sensitive fluorescent detection of microRNA cancer biomarkers, Biosens. Bioelectron. 77 (2016) 416–420.
[5] L. Tian, J. Qi, X. Ma, X. Wang, C. Yao, W. Song, et al., A facile DNA strand displacement reaction sensing strategy of electrochemical biosensor based on N-carboxymethyl chitosan/molybdenum carbide nanocomposite for microRNA-21 detection, Biosens. Bioelectron. 122 (2018) 43–50.
[6] P. Zhang, Z. Li, H. Wang, Y. Zhuo, R. Yuan, Y. Chai, DNA nanomachine-based regenerated sensing platform: a novel electrochemiluminescence resonance energy transfer strategy for ultra-high sensitive detection of microRNA from cancer cells, Nanoscale 9 (2017) 2310–2316.
[7] J. Zhang, L. Wang, M. Hou, Y. Xia, W. He, A. Yan, et al., A ratiometric electrochemical biosensor for the exosomal microRNAs detection based on bipedal DNA walkers propelled by locked nucleic acid modified toehold mediate strand displacement reaction, Biosens. Bioelectron. 102 (2017) 33–40.
[8] H. Liao, Y. Zhou, Y. Chai, R. Yuan, An ultrasensitive electrochemiluminescence biosensor for detection of MicroRNA by in-situ electrochemically generated copper nanoclusters as luminophore and $TiO_2$ as coreaction accelerator, Biosens. Bioelectron. 114 (2018) 10–14.
[9] Y. Yu, J. Wang, M. Zhao, L. Hong, Y. Chai, R. Yuan, et al., Target-catalyzed hairpin assembly and intramolecular/intermolecular co-reaction for signal amplified electrochemiluminescent detection of microRNA, Biosens. Bioelectron. 77 (2016) 442–450.
[10] L. Wang, T. Meng, G. Yu, S. Wu, J. Sun, H. Jia, et al., A label-free electrochemical biosensor for ultra-sensitively detecting telomerase activity based on the enhanced catalytic currents of acetaminophen catalyzed by Au nanorods, Biosens. Bioelectron. 124–125 (2019) 53–58.
[11] T. Meng, A. Nsabimana, T. Zeng, H. Jia, S. An, H. Wang, Y. Zhang, Preparation of Pt anchored on cerium oxide and ordered mesoporous carbon tri-component composite for electrocatalytic oxidation of adrenaline, Mater. Sci. Eng. C 110 (2020) 110747.
[12] L. Wang, T. Meng, H. Jia, Y. Feng, T. Gong, H. Wang, et al., Electrochemical study of hydrazine oxidation by leaf-shaped copper oxide loaded on highly ordered mesoporous carbon composite, J. Colloid Interface Sci. 549 (2019) 98–104.
[13] M. Li, J. Yang, M. Lu, Y. Zhang, X. Bo, Facile design of ultrafine $Co_7Fe_3$ nanoparticles coupled with nitrogen-doped porous carbon nanosheets for non-enzymatic glucose detection, J. Colloid Interface Sci. 555 (2019) 449–459.
[14] T. Meng, H. Jia, H. Ye, T. Zeng, X. Yang, H. Wang, et al., Facile preparation of $CoMoO_4$ nanorods at macroporous carbon hybrid electrocatalyst for nonenzymatic glucose detection, J. Colloid Interface Sci. 560 (2020) 1–10.
[15] L. Wang, T. Meng, J. Sun, S. Wu, M. Zhang, H. Wang, et al., Development of Pd/Polyoxometalate/nitrogen-doping hollow carbon spheres tricomponent nanohybrids: a selective electrochemical sensor for acetaminophen, Anal. Chim. Acta 1047 (2019) 28–35.
[16] H. Tran, B. Piro, S. Reisberg, H. Duc, M. Pham, Antibodies directed to RNA/DNA hybrids: an electrochemical immunosensor for microRNAs detection using graphene-composite electrodes, Anal. Chem. 85 (2013) 8469–8474.
[17] P. Ramnani, Y. Gao, M. Ozsoz, A. Mulchandani, Electronic detection of microRNA at attomolar level with high specificity, Anal. Chem. 85 (2013) 8061–8064.
[18] H. Tran, B. Piro, S. Reisberg, L. Tran, H. Duc, M. Pham, Label-free and reagentless electrochemical detection of microRNAs using a conducting polymer nanostructured by carbon nanotubes: application to prostate cancer biomarker miR-141, Biosens. Bioelectron. 49 (2013) 164–169.
[19] M. Labib, N. Khan, S. Ghobadloo, J. Cheng, J. Pezacki, M. Berezovski, Three-mode electrochemical sensing of ultralow microRNA levels, J. Am. Chem. Soc. 135 (2013) 3027–3038.
[20] H. Tran, B. Piro, S. Reisberg, L. Nguyen, H. Duc, M. Pham, An electrochemical ELISA-like immunosensor for miRNAs detection based on screen-printed gold electrodes modified with reduced graphene oxide and carbon nanotubes, Biosens. Bioelectron. 62 (2014) 25–30.
[21] H. Yin, Y. Zhou, H. Zhang, X. Meng, S. Ai, Electrochemical determination of microRNA-21 based on graphene, LNA integrated molecular beacon, AuNPs and biotin multifunctional bio bar codes and enzymatic assay system, Biosens. Bioelectron. 33 (2012) 247–253.
[22] H. Dong, S. Jin, H. Ju, K. Hao, L. Xu, H. Lu, et al., Trace and label-free microRNA detection using oligonucleotide encapsulated silver nanoclusters as probes, Anal. Chem. 84 (2012) 8670–8674.
[23] L. Liu, S. Zhu, Y. Wei, X. Liu, S. Jiao, J. Yang, Ultrasensitive detection of miRNA-155 based on controlled fabrication of AuNPs@$MoS_2$ nanostructures by atomic layer deposition, Biosens. Bioelectron. 144 (2019) 111660.
[24] T. Meng, H. Jia, S. An, H. Wang, X. Yang, Y. Zhang, Pd nanoparticles-DNA layered nanoreticulation biosensor based on target catalytic hairpin assembly for ultrasensitive and selective biosensing of microRNA-21 Sens, Actuators B 323 (2020) 128621.
[25] B. Yang, S. Zhang, X. Fang, J. Kong, Double signal amplification strategy for ultrasensitive electrochemical biosensor based on nuclease and quantum dot-DNA nanocomposites in the detection of breast cancer 1 gene mutation, Biosens. Bioelectron. 142 (2019) 111544.
[26] H. Rezaei, M. Motovali-Bashi, S. Radfar, An enzyme-free electrochemical biosensor for simultaneous detection of two hemophilia A biomarkers: combining target recycling with quantum dots-encapsulated metal-organic frameworks for signal amplification, Anal. Chim. Acta 1092 (2019) 66–74.
[27] L. Yu, P. He, Y. Xu, X. Kou, Z. Yu, X. Xie, et al., Manipulations of DNA four-way junction architecture and DNA modified $Fe_3O_4$@Au nanomaterials for the detection of miRNA, Sens. Actuators, B 313 (2020) 128015.
[28] W. Tian, P. Li, W. He, C. Liu, Z. Li, Rolling circle extension-actuated loop-mediated isothermal amplification (RCA-LAMP) for ultrasensitive detection of microRNAs, Biosens. Bioelectron. 128 (2019) 17–22.
[29] T. Li, X. Wu, G. Tao, H. Yin, J. Zhang, F. Liu, et al., A simple and non-amplification platform for femtomolar DNA and microRNA detection by combining automatic gold nanoparticle enumeration with target-induced strand-displacement, Biosens. Bioelectron. 105 (2018) 137–142.
[30] H. Xu, D. Wu, Y. Zhang, H. Shi, C. Ouyang, F. Li, et al., RCA-enhanced multi-functional molecule beacon-based strand-displacement amplification for sensitive microRNA detection, Sens. Actuators, B 258 (2018) 470–477.
[31] M. Yao, X. Lv, Y. Deng, M. Rasheed, Specific and simultaneous detection of micro RNA 21 and let-7a by rolling circle amplification combined with lateral flow strip, Anal. Chim. Acta 1055 (2019) 115–125.
[32] T. Meng, D. Zhao, H. Ye, Y. Feng, H. Wang, Y. Zhang, Construction of an ultrasensitive electrochemical sensing platform for microRNA-21 based on interface impedance spectroscopy, J. Colloid Interface Sci. 578 (2020) 164–170.
[33] H. Cheng, W. Li, S. Duan, J. Peng, J. Liu, W. Ma, et al., Mesoporous silica containers and programmed catalytic hairpin assembly/hybridization chain reaction based electrochemical sensing platform for microRNA ultrasensitive detection with low background, Anal. Chem. 91 (2019) 10672–10678.
[34] J. Zhuang, W. Lai, G. Chen, D. Tang, A rolling circle amplification-based DNA machine for miRNA screening coupling catalytic hairpin assembly with DNAzyme formation, Chem. Commun. 50 (2014) 2935–2938.
[35] P. Ling, J. Lei, L. Jia, H. Ju, Platinum nanoparticles encapsulated metal–organic frameworks for the electrochemical detection of telomerase activity, Chem. Commun. 52 (2016) 1226–1229.
[36] T. Meng, L. Wang, H. Jia, T. Gong, Y. Feng, R. Li, et al., Facile synthesis of platinum-embedded zirconia/porous carbons tri-component nanohybrids from metal-organic framework and their application for ultra-sensitively detection of methyl parathion, J. Colloid Interface Sci. 536 (2019) 424–430.
[37] Z. Xu, C. Xu, L. Yang, Pt@UiO-66 heterostructures for highly selective detection of $H_2O_2$ with an extended linear range, Anal. Chem. 87 (2015) 3438–3444.
[38] Y. Zhang, X. Bo, A. Nsabimana, C. Han, M. Li, L. Guo, Electrocatalytically active cobalt-based metal–organic framework with incorporated macroporous carbon composite for electrochemical applications, J. Mater. Chem. 3 (2015) 732–738.
[39] L. Wang, T. Meng, C. Chen, Y. Fan, Q. Zhang, H. Wang, et al., Facile synthesis of ZnCo-ZIFs-derived $Zn_xCo_{3-x}O_4$ hollow polyhedron for efficient oxygen evolution reduction, J. Colloid Interface Sci. 532 (2018) 650–656.
[40] M. Li, P. Dong, Y. Zhang, Facile design and synthesis of ultrafine FeCo nanocrystallines coupled with porous carbon nanosheets as high efficiency non-enzymatic glucose sensor, J. Alloys Compd. 810 (2019) 151927.
[41] H. Jia, M. Zhang, T. Meng, S. An, H. Wang, Y. Zhang, Facile synthesis of Fe, Co bimetal embedded nanoporous carbon polyhedron composites for an efficient oxygen evolution reaction, J. Colloid Interface Sci. 563 (2020) 189–196.
[42] L. Wang, Q. Teng, X. Sun, Y. Chen, Y. Wang, H. Wang, et al., Facile synthesis of metal-organic frameworks/ordered mesoporous carbon composites with enhanced electrocatalytic ability for hydrazine, J. Colloid Interface Sci. 512 (2018) 127–133.
[43] T. Saleh, Isotherm, kinetic, and thermodynamic studies on Hg(II) adsorption from aqueous solution by silica- multiwall carbon nanotubes, Environ. Sci. Pollut. Res. 22 (2015) 16721–16731.
[44] T. Saleh, M. Tuzen, A. Sari, Polyamide magnetic palygorskite for the simultaneous removal of Hg(II) and methyl mercury; with factorial design analysis, J. Environ. Manag. 211 (2018) 323–333.
[45] T. Saleh, Mercury sorption by silica/carbon nanotubes and silica/activated carbon: a comparison study, J. Water Supply Res. Technol. - Aqua 64 (2015) 892–903.
[46] Y. Zhang, X. Bo, A. Nsabimana, A. Munyentwali, C. Han, M. Li, et al., Green and facile synthesis of an Au nanoparticles@polyoxometalate/ordered mesoporous carbon tri-component nanocomposite and its electrochemical applications, Biosens. Bioelectron. 66 (2015) 191–197.
[47] T. Zhang, M. Liu, Q. Zhang, Y. Wang, X. Kong, L. Wang, et al., Sensitive determination of chlorogenic acid in pharmaceutical products based on the decoration of 3D macroporous carbon with Au nanoparticles via polyoxometalates, Analyst 142 (2017) 2603–2609.
[48] X. Kong, Y. Wang, Q. Zhang, T. Zhang, Q. Teng, L. Wang, et al., Ex-situ decoration of ordered mesoporous carbon with palladium nanoparticles via polyoxometalates and for sensitive detection of acetaminophen in pharmaceutical products, J. Colloid Interface Sci. 505 (2017) 615–621.
[49] L. Wang, T. Meng, D. Zhao, H. Jia, S. An, X. Yang, et al., An enzyme-free electrochemical biosensor based on well monodisperse Au nanorods for ultrasensitive detection of telomerase activity, Biosens. Bioelectron. 148 (2020) 111834.
[50] L. Wang, T. Meng, L. Liang, J. Sun, S. Wu, H. Wang, et al., Fabrication of amine-functionalized metal-organic frameworks with embedded palladium nanoparticles for highly sensitive electrochemical detection of telomerase activity, Sensor. Actuator. B 278 (2019) 133–139.

[51] D. Jiang, G. Fang, Y. Tong, X. Wu, Y. Wang, D. Hong, et al., Multifunctional Pd@UiO-66 catalysts for continuous catalytic upgrading of ethanol to n-butanol, ACS Catal. 8 (2018) 11973–11978.
[52] T. Saleh, Naeemullah, M. Tuzen, A. Sari, Polyethylenimine modified activated carbon as novel magnetic adsorbent for the removal of uranium from aqueous solution, Chem. Eng. Res. Des. 117 (2016) 218–227.
[53] S. Adio, M. Omar, M. Asif, T. Saleh, Arsenic and selenium removal from water using biosynthesized nanoscale zero-valent iron: a factorial design analysis, Process Saf. Environ. Protect. 107 (2017) 518–527.
[54] T. Saleh, Simultaneous adsorptive desulfurization of diesel fuel over bimetallic nanoparticles loaded on activated carbon, J. Clean. Prod. 172 (2018) 2123–2132.
[55] T. Saleh, Nanocomposite of carbon nanotubes/silica nanoparticles and their use for adsorption of Pb(II): from surface properties to sorption mechanism, Desalin. Water Treat. 57 (2016) 10730–10744.
[56] D. Jiang, G. Fang, Y. Tong, X. Wu, Y. Wang, D. Hong, et al., Multifunctional Pd@UiO-66 catalysts for continuous catalytic upgrading of ethanol to n-butanol, ACS Catal. 8 (2018) 11973–11978.
[57] F. Li, R. Li, Y. Feng, T. Gong, M. Zhang, L. Wang, et al., Facile synthesis of Au-embedded porous carbon from metal-organic frameworks and for sensitive detection of acetaminophen in pharmaceutical products, Mater. Sci. Eng. C 95 (2019) 78–85.
[58] Y. Cheng, J. Lei, Y. Chen, H. Ju, Highly selective detection of microRNA based on distance-dependent electrochemiluminescence resonance energy transfer between CdTe nanocrystals and Au nanoclusters, Biosens. Bioelectron. 51 (2014) 431–436.
[59] J. Li, Z. Chen, Y. Xiang, L. Zhou, T. Wang, Z. Zhang, et al., An electrochemical biosensor for double-stranded Wnt7B gene detection based on enzymatic isothermal amplification, Biosens. Bioelectron. 86 (2016) 75–82.
[60] Q. Feng, Y. Shen, M. Li, Z. Zhang, W. Zhao, J. Xu, et al., Dual-wavelength electrochemiluminescence ratiometry based on resonance energy transfer between Au nanoparticles functionalized g-$C_3N_4$ nanosheet and $Ru(bpy)_3^{(2+)}$ for microRNA Detection, Anal. Chem. 88 (2017) 937–944.
[61] N. Ying, T. Sun, Z. Chen, G. Song, B. Qi, S. Bu, et al., Colorimetric detection of microRNA based hybridization chain reaction for signal amplification and enzyme for visualization, Anal. Biochem. 528 (2017) 7–12.
[62] Q. Tian, Y. Wang, R. Deng, L. Lin, Y. Liu, J. Li, Carbon nanotube enhanced label-free detection of microRNAs based on hairpin probe triggered solid-phase rolling-circle amplification, Nanoscale 7 (2014) 987–993.
[63] W. Wang, T. Kong, D. Zhang, J. Zhang, G. Cheng, Label-free microRNA detection based on fluorescence quenching of gold nanoparticles with a competitive hybridization, Anal. Chem. 87 (2015) 10822–10829.
[64] M. Kamal, M. Islam, M. Haque, S. Tanaka, V. Gopalan, G. Alici, et al., Gold-loaded nanoporous superparamagnetic nanocubes for catalytic signal amplification in detecting miRNA, Chem. Commun. 53 (2017) 8231–8234.
[65] Y. Yu, Z. Chen, L. Shi, F. Yang, J. Pan, B. Zhang, D. Sun, Ultrasensitive electrochemical detection of microRNA based on an arched probe mediated isothermal exponential amplification, Anal. Chem. 86 (2014) 8200–8205.
[66] N. Xia, L. Zhang, G. Wang, Q. Feng, L. Liu, Label-free and sensitive strategy for microRNAs detection based on the formation of boronate ester bonds and the dual-amplification of gold nanoparticles, Biosens. Bioelectron. 47 (2013) 461–466.
[67] D. Zhu, W. Liu, D. Zhao, Q. Hao, J. Li, J. Huang, et al., Label-free electrochemical sensing platform for microRNA-21 detection using thionine and gold nanoparticles Co-functionalized $MoS_2$ nanosheet, ACS Appl. Mater. Interfaces 9 (2017) 35597–35603.
[68] L. Zhou, W. Jian, Z. Chen, J. Li, T. Wang, Z. Zhang, et al., A universal electrochemical biosensor for the highly sensitive determination of microRNAs based on isothermal target recycling amplification and a DNA signal transducer triggered reaction, Microchim. Acta 184 (2017) 1305–1313.
[69] S. Liu, Z. Yang, Y. Chang, Y. Chai, R. Yuan, An enzyme-free electrochemical biosensor combining target recycling with $Fe_3O_4/CeO_2$@Au nanocatalysts for microRNA-21 detection, Biosens. Bioelectron. 119 (2018) 170–175.
[70] D. Zhu, W. Liu, W. Cao, J. Chao, S. Su, L. Wang, et al., Multiple amplified electrochemical detection of microRNA-21 using hierarchical flower-like gold nanostructures combined with gold-enriched hybridization chain reaction, Electroanalysis 30 (2018) 1349–1356.
[71] J. Liu, Z. Tang, J. Zhang, Y. Chai, Y. Zhuo, R. Yuan, Morphology-controlled 9,10-diphenylanthracene nanoblocks as electrochemiluminescence emitters for microRNA detection with one-step DNA walker amplification, Anal. Chem. 90 (2018) 5298–5305.
[72] W. Cai, S. Xie, Y. Tang, Y. Chai, R. Yuan, J. Zhang, A label-free electrochemical biosensor for microRNA detection based on catalytic hairpin assembly and in situ formation of molybdophosphate, Talanta 163 (2017) 65–71.
[73] Y. Yu, J. Wang, M. Zhao, L. Hong, Y. Chai, R. Yuan, et al., Target-catalyzed hairpin assembly and intramolecular/intermolecular co-reaction for signal amplified electrochemiluminescent detection of microRNA, Biosens. Bioelectron. 77 (2016) 442–450.